Actuation Frequency Modeling and Prediction for Shape Memory Alloy Actuators

Xiaolong Liu , Hui Liu , and Jindong Tan , *Member, IEEE*

Abstract—**This article proposes a numerical model to predict actuation frequencies (strain-cycling frequencies) for 1-D shape memory alloy (SMA) actuators. The numerical model is designed by comprehensively considering the factors that significantly affect an SMA actuator's strain-cycling frequency, i.e., heat convection methods, constant or nonconstant bias loads, and Joule heating methods. For computing strain cycles of SMA actuators, we develop a computation framework that effectively integrates an SMA constitutive model, a phase transformation kinetic model, stress-strain models for different types of bias stress, and a heat transfer model of SMA wires. The strain and temperature rates are formulated by nonlinear ordinary differential equations. The strain and temperature cycles can be accurately approximated by numerical iterative methods. Experimental verification was conducted to investigate the effectiveness of the proposed model. By initially identifying the SMA characteristic parameters, we employed Latin hypercube sampling method to generate 30 sets of design parameters for comparing the predicted and measured actuation frequencies. In addition, we investigated how the uncertainty of premeasured SMA characteristic parameters affect the numerical prediction of actuation frequency by conducting sensitivity analysis. The experiments demonstrate 0.7%–9.03% and 2.65%–17.57% differences between predicted and measured actuation frequencies for constant bias loads and spring bias loads, respectively.**

Index Terms—**Actuation frequency, numerical model, shape memory alloy (SMA), SMA actuator.**

I. INTRODUCTION

SHAPE memory alloys (SMAs) have been attracting vast attention of researchers to develop novel mechatronic devices [1] due to the materials' unique features, which include highly adaptive, high power-to-weight ratio, compact, low driving voltages, great biocompatibility, and being capable of converting thermal energy to mechanical work with large plastic deformation [2]. These features enable SMAs an ideal actuator in biomedical applications, such as artificial muscles [3], active catheters [4], vascular stents [5], and deformable surgical instruments [6]. SMAs also have been widely applied in robotics [7], automotive industry [8], and aerospace [9]. However, one major challenge is to develop SMA actuators with desired actuation frequencies.

SMA actuation frequency (or strain-cycling frequency) is determined by the cycle of material phase transformation between martensite and austenite, which is mainly affected by heat convection rate, SMA heating strategy, and bias stress [10]. Although the nature of SMA actuator limits the actuation frequency at low level, research efforts have been made to improve and optimize the designs for various applications that require low-frequency actuation. A complete actuation cycle adds up the duration of heating process and cooling process. One most common way to expedite cooling process is to design forced convection systems, e.g., by using active air [11] or water [12] flow, heat sink [13], and semiconductor module [14]. An alternate strategy to improve actuation frequency is to employ higher voltages or currents to activate SMA actuators [15], which can significantly reduce the duration of heating process. Instead of reaching the maximum strain in each actuation cycle, partial-strain actuation can also improve the actuation frequency by sacrificing SMA stroke distance [16]. Bias loads of SMA actuators, such as springs and antagonistic SMA wires [17], [18], not only affect phase transformation temperatures, but they can also change the strain rate of elongation during cooling process and subsequently impact on actuation frequency [19]. Practically, when designing SMA actuators, there is a need for engineers to know the maximum attainable working frequency by adopting different combinations of the abovementioned design factors before implementing a prototype or conducting an experiment [20].

The goal of our research is to develop an effective model to serve as a design tool for predicting actuation frequency of SMA actuators. The prediction of an SMA actuator's behavior involves analyzing SMA heat transfer [21], [22] and phase transformation, which is characterized by constitutive models [10], [23], [24]. The highly nonlinear relationships between SMA parameters (temperature T, strain ϵ, bias stress σ) compel most researchers to conduct experimental investigations for understanding an SMA actuator's response time based on various testing conditions such as active cooling [25], fast heating [26], and applied stress [27]. An early work develops an analytical model to examine temperature response of SMA wires under
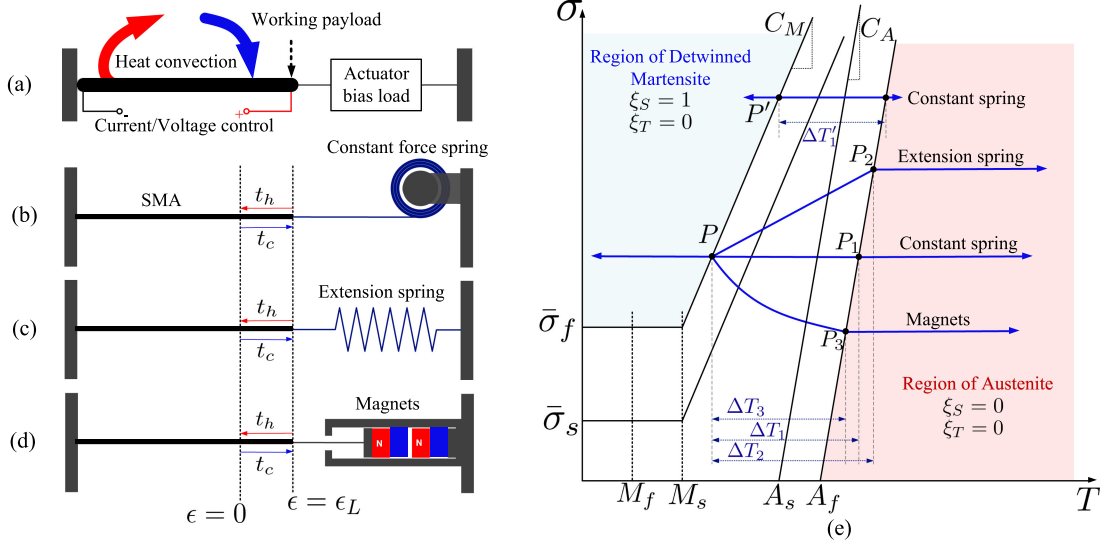
Fig. 1. Configuration and working principle of 1-D SMA actuators. (a) Typical configuration of 1-D SMA actuators. (b) Constant bias load. (c) Increasing bias load during heating process. (d) Decreasing bias load during heating process. (e) Illumination of effects on SMA phase transformation by using different types of bias loads according to Brinson's critical stress model [23]. M_f, M_s, A_f, and A_s are SMA phase transformation temperatures under zero stress. $\bar{\sigma}_f$ and $\bar{\sigma}_s$ are critical stresses when $T < M_s$.

different cooling conditions [14]. But this article simplifies the model with zero-stress condition, which is incapable of applying to SMA actuators.

In this article, we develop a numerical model for predicting actuation frequency of 1-D SMA actuators that consist of an SMA wire and bias loads. This model is able to estimate actuation frequencies for 1-D SMA actuators with various design configurations, including but not limited to different bias loads, natural/forced heat convection, and Joule heating strategies, etc. We conduct experimental tests to evaluate effectiveness of the proposed model. For investigating how predetermined design parameters affect the perdition results, we performed sensitivity analysis on 12 property parameters of SMA wires. The experiment results initially reveal that the numerical model is capable of predicting the actuation frequency of 1-D SMA actuators within the testing range of 0.06–0.2 Hz. The percentage differences between the numerically predicted and experimentally measured actuation frequencies are in the range of 0.7%–9.03% and 2.65%–17.57% for constant bias loads and spring bias loads, respectively. To the best of authors' knowledge, this article makes the very first effort to study the performance of a numerical model for predicting actuation frequency of 1-D SMA actuators.

II. 1-D SMA ACTUATOR

Fig. 1(a) shows a typical configuration of 1-D SMA actuators. The SMA wire is initially prestressed at the phase of detwinned martensite (M_d) by a bias load. The actuation for each cycle involves the SMA wire contraction by heating and wire elongation by cooling and bias stress. The heat generated by Joule heating in the SMA wire induces the phase of austenite (A), which activates internal driving energy to contract the wire and recover its original length (shape memory effect). The phase

transformation $M_d \rightarrow A$ enables the wire to overcome the bias load and the working payload. By ceasing Joule heating and employing various heat convection strategies, the wire cools down and subsequently the bias load can stretch the wire to its initial length ($A \rightarrow M_d$) for completing one actuation cycle.

The strain-cycling frequency f is determined by duration of heating (t_h) and cooling (t_c), which is represented by

$$f = \frac{1}{t_h + t_c}. \tag{1}$$

To change f in an SMA actuator design, most research studies have focused on developing heat convection systems and/or Joule heating strategies. However, an actuator's bias load can also significantly affect f. Fig. 1(b)–(d) demonstrates three different types of bias loads: constant force spring, which provides constant stress on the SMA wire during actuation [see Fig. 1(b)]; extension spring, which increases the applied stress as the SMA wire contracts toward strain $\epsilon = 0$, and decreases the applied stress as the SMA wire is elongated toward $\epsilon = \epsilon_L$, where ϵ_L is the maximum recoverable strain [see Fig. 1(c)]; and magnetic bias load, which behaves opposite to extension springs, i.e., increasing stress during SMA elongation and decreasing stress during SMA contraction [see Fig. 1(d)]. Under the same condition of heat convection and Joule heating, the three bias loads demonstrate different effects in Brinson's critical stress model [23], as illustrated in Fig. 1(e). Assuming that the bias loads provide the same initial stress σ_P at point P, the lines $P - P_1, P - P_2$, and $P - P_3$ show different temperature intervals $\Delta T_3 < \Delta T_1 < \Delta T_2$, which are required for phase transformation $M_d \leftrightarrow A$ in SMA actuators with corresponding bias loads. Even with the same type of bias load, such as a constant spring with different stress level $\sigma_{P'}$, the phase transformation temperature interval $\Delta T_1'$ can be much smaller than ΔT_1 due to

$C_M < C_A$, and consequently the actuator can have a higher attainable f. Therefore, for accurately predicting SMA actuators' actuation frequencies, it is necessary to consider bias loads in addition to heat convection and Joule heating.

III. MODELING OF STRAIN-CYCLING FREQUENCY

The actuation behavior of SMAs characterized by thermo-mechancial constitutive model involves nonlinearly coupled relationships among stress σ, strain ϵ, material's martensite fraction ξ, and temperature T. The research objective of this article is to model the strain-cycling frequency that requires a direct connection between strain ϵ and time t. To decouple ϵ from the SMA constitutive model, we develop a heat transfer model for SMA actuators to obtain an additional relationship between martensite fraction ξ and temperature T. By combing the SMA constitutive model, phase transformation kinetics, and the heat transfer model, we are able to formulate strain rate $\dot{\epsilon}$ and temperature rate $\dot{T}$ in a system of first order differential equations. Thereby, numerical methods can be applied to solve relations of $\epsilon - t$ and $T - t$.

A. 1-D SMA Constitutive Model With Bias Loads

1) Constitutive Model: SMAs' thermomechanical behavior has been extensively studied since 1980s. Based on thermodynamics theory, Tanaka [28] initially developed a phenomenological constitutive model by minimizing free energy in energy balance equation and Clausium–Duhem inequality with a set of variables (σ, ϵ, T, ξ) and described the phase transformation kinetics by an exponential function. Two other representative works conducted by Liang-Rogers [10] and Brinson [23] extended the Tanaka's model by improving the modeling accuracy of phase transformation kinetics. In this article, we adopt the rate form of the SMA constitutive model in the following equation:

$$\dot{\sigma} = D(\xi)\dot{\epsilon} + \Theta\dot{T} + \Omega(\xi)\dot{\xi} \qquad (2)$$

where $D(\xi)$ presents the Young's modulus; Θ is the thermal coefficient of expansion and $\Omega(\xi)$ is transformation tensor. $D(\xi)$ and $\Omega(\xi)$ are functions of martensite fraction ξ

$$D(\xi) = D_A + (D_M - D_A)\xi \qquad (3)$$
$$\Omega(\xi) = -\epsilon_L D(\xi) \qquad (4)$$

where D_A and D_M are the Young's moduli when SMA is in the phases of austenite ($\xi = 0$) and martensite ($\xi = 1$), respectively. ϵ_L denotes the maximum recoverable strain.

2) Phase Transformation Kinetics Characterization: In the 1-D SMA constitutive model (2), the martensite fraction ξ is used to characterize the phase transformation kinetics between austenite and detwinned martensite. Governed by chemical free energy, ξ can be approximated as a function of temperature T and stress σ. The modeling accuracy of kinetic law can significantly affect the prediction results of 1-D SMA behavior [29]. Considering that both temperature-induced matensite ξ_T and stress-induced matensite ξ_S exist during cooling process of 1-D SMA actuators, we employ Brinson's phase transformation

kinetic model [23], which is illustrated in Fig. 1(e) (black lines), to represent the matensite fraction $\xi = \xi_T + \xi_S$.

a) Design considerations of 1-D SMA actuators: This article considers 1-D SMA actuators to achieve full strain range $0 \sim \epsilon_L$. Based on a specific SMA material, the yielding stress σ_y, critical stress $\bar{\sigma}_f$, and working payload σ_w can be determined. To elongate the SMA wire to the strain ϵ_L as an initial condition, the bias stress σ should be in the range of $\bar{\sigma}_f + \sigma_w < \sigma < \sigma_y$, which is indicated in the blue region in Fig. 1(e). Thus, $\xi_S = 1$ and $\xi_T = 0$ are the initial martensite fractions for the heating process $M_d \to A$. The cooling process $A \to M_d$ is initialized in the red region of Fig. 1(e), where $\xi_S = 0$ and $\xi_T = 0$.

According to the initial conditions of ξ_S and ξ_T for heating and cooling processes, the phase transformation kinetics ξ can be modeled in (5) and (7). Due to stress-induced martensite transformation in the SMA actuators, the temperature-induced martensite fraction can be considered as zero ($\xi_T = 0$), which means we can use ξ_S to represent ξ.

b) Cooling process $A \to M_d$: For $T > M_s$ and $\bar{\sigma}_s + C_M(T - M_s) < \sigma < \bar{\sigma}_f + C_M(T - M_s)$, ξ is modeled as

$$\xi = \frac{1}{2}\cos\{a_M[\sigma - \bar{\sigma}_f - C_M(T - M_s)]\} + \frac{1}{2} \qquad (5)$$

where

$$a_M = \frac{\pi}{\bar{\sigma}_s - \bar{\sigma}_f}. \qquad (6)$$

c) Heating process $M_d \to A$: For $T > A_s$ and $C_A(T - A_f) < \sigma < C_A(T - A_s)$, ξ can be modeled as

$$\xi = \frac{1}{2}\left\{\cos\left[a_A\left(T - A_s - \frac{\sigma}{C_A}\right)\right] + 1\right\} \qquad (7)$$

where

$$a_A = \frac{\pi}{A_f - A_s}. \qquad (8)$$

d) Rate of ξ: The rate form of ξ can, thus, be derived in (9) and (10) by taking derivatives on (5) and (7).

$A \to M_d$:

$$\dot{\xi} = -\frac{1}{2}\sin\{a_M[\sigma - \bar{\sigma}_f - C_M(T - M_s)]\}(a_M\dot{\sigma} - a_M C_M\dot{T}). \qquad (9)$$

$M_d \to A$:

$$\dot{\xi} = -\frac{1}{2}\sin\left[a_A(T - A_s) - \frac{a_A}{C_A}\sigma\right]\left(a_A\dot{T} - \frac{a_A}{C_A}\dot{\sigma}\right). \qquad (10)$$

By substituting (9) and (10) in (2), we can observe that the constitutive model is governed by σ, T, and ϵ. For the case of constant bias load as shown in Fig. 1(b), the constitutive equation immediately describes $\epsilon - T$. However, situations are more complicated to employ nonconstant bias loads.

3) $\sigma - \epsilon$ Relation Under Nonconstant Bias Loads: Nonconstant bias loads, as shown in Fig. 1(c) and (d), vary applied stress on the SMA wires as strain changes. For the case of using an extension spring as the bias load, the stress-strain relationship can be formulated as

$$\sigma = \frac{kL}{s}(\epsilon_L - \epsilon) + \frac{F_i}{s} \qquad (11)$$

where k is the spring rate; L is the SMA wire length at the phase of austenite; s is the cross-sectional area of the SMA wire; and F_i is the initial tension of an extension spring. The rate form of (11) is expressed as

$$\dot{\sigma} = -\frac{kL}{s}\dot{\epsilon}. \tag{12}$$

For the case of using magnetic bias load, by assuming the cylindrical magnets are axially magnetized, the stress-strain relationship can be modeled by a polynomial curve. Without loss of generality, to make this article concise, we only discuss extension springs as the example of nonconstant bias load.

4) Strain Temperature $\epsilon - T$ Equations:

a) Constant bias load: With constant bias load, $\dot{\sigma}$ becomes 0 in (2). We also substitute $\sigma = \sigma_c$ and $\dot{\sigma} = 0$ in (5), (7), (9), and (10), where σ_c denotes the constant bias stress. The $\epsilon - T$ equations for constant bias loads can be formulated as

$$D\dot{\epsilon} + (\Theta + \Omega\bar{W})\dot{T} = 0, \quad A \rightarrow M_d \tag{13}$$

$$D\dot{\epsilon} + (\Theta + \Omega\bar{H})\dot{T} = 0, \quad M_d \rightarrow A \tag{14}$$

where D and Ω are functions of temperature T according to (3), (4), (5), (7); $\bar{W}$ and $\bar{H}$ are also functions of T, and represented as

$$\bar{W} = \frac{a_M C_M}{2} \sin\{a_M[\sigma_c - \bar{\sigma}_f - C_M(T - M_s)]\} \tag{15}$$

$$\bar{H} = -\frac{a_A}{2} \sin\left[a_A(T - A_s) - \frac{a_A}{C_A}\sigma_c\right]. \tag{16}$$

b) Non-constant bias load: For an extension spring bias load, by substituting (12) in (2), we have

$$\left(D(\xi) + \frac{kL}{s}\right)\dot{\epsilon} + \Theta\dot{T} + \Omega(\xi)\dot{\xi} = 0. \tag{17}$$

For the existence of σ and/or $\dot{\sigma}$ in (5), (7), (9), and (10), we apply (11) and/or (12) to substitute σ and/or $\dot{\sigma}$ with ϵ and/or $\dot{\epsilon}$. Thus, the strain-temperature relation can be derived as:

$A \rightarrow M_d$

$$\left(D + \frac{kL}{s} + \Omega W W_\epsilon\right)\dot{\epsilon} + (\Theta - \Omega W W_T)\dot{T} = 0. \tag{18}$$

$M_d \rightarrow A$

$$\left(D + \frac{kL}{s} + \Omega H H_\epsilon\right)\dot{\epsilon} + (\Theta + \Omega H a_A)\dot{T} = 0 \tag{19}$$

where W and H are functions of ϵ and T, and are represented as

$$W = -\frac{1}{2}\sin\left\{a_M\left[\frac{kL}{s}(\epsilon_L - \epsilon)\right.\right.$$
$$\left.\left. + \frac{F_i}{s} - \bar{\sigma}_f - C_M(T - M_s)\right]\right\} \tag{20}$$

$$H = -\frac{1}{2}\sin\left\{a_A(T - A_s) - \frac{a_A}{C_A}\left[\frac{kL}{s}(\epsilon_L - \epsilon) + \frac{F_i}{s}\right]\right\}. \tag{21}$$

W_ϵ, W_T, and H_ϵ are denoted as

$$W_\epsilon = -\frac{a_M k L}{s}, \; W_T = a_M C_M, \; H_\epsilon = \frac{a_A k L}{C_A s}. \tag{22}$$

It is worth noting that (13), (14) and (18), (19) are nonlinear first-order ordinary differential equations (ODEs) with two variables ϵ and T. If we can compute the value of $\dot{\epsilon}$ and $\dot{T}$ during the motion of SMA actuators, we will be able to numerically estimate the required time for heating and cooling in each cycle. For doing this, however, another set of $\epsilon - T$ relationships will be needed.

B. 1-D SMA Heat Transfer Differential Equation

From the perspective of energy balance for 1-D SMA wires, the rate of heat flow is approximately equal to the rate of energy change when the wire's length-diameter ratio is very large; the Biot number B_i is smaller than 0.1; and the wire boundary condition is uniform [14]. These assumptions are valid for most 1-D SMA applications. Therefore, the heat transfer equation for 1-D SMA actuators is formulated as

$$mc_p\dot{T} - m\Delta h\dot{\xi} = I^2 R - hS(T - T_\infty) \tag{23}$$

where m is the wire mass; c_p is specific heat in constant pressure of the SMA; Δh is the latent heat of transformation, which is specified in an SMA's datasheet; h is heat convection coefficient; S is the surface area of the SMA wire; T_∞ is the ambient temperature; I is the current input; and the wire electrical resistance R is a function of martensite fraction

$$R(\xi) = \frac{L'}{s}(\rho_A + \xi(\rho_M - \rho_A)). \tag{24}$$

$L' = L(1 + \epsilon)$; ρ_A and ρ_M are electrical resistivity of SMA wires at the phase of austenite and martensite, respectively [30].

In (23), the left-hand side represents the SMA energy change according to temperature change and the rate of SMA phase transformation. The right-hand side represents the heat transfer rate that is influenced the heating method $I^2 R$ and the convective cooling method $-hS(T - T_\infty)$. During cooling process, the term $I^2 R$ is omitted since $I = 0$.

By using (5), (7), (9), (10), (11), (12), the heat transfer differential equation (23) can provide another set of ODEs with ϵ and T as variables to be paired with (13) and (14) for constant bias loads; (18) and (19) for nonconstant bias loads.

1) Heat Transfer Equation for Constant Bias Load SMA Actuator: Under the condition of constant bias load, the SMA heat transfer equation (23) is reformulated in (25) for describing the heating and cooling processes

$$\dot{T} = \begin{cases} \frac{-hS(T-T_\infty)}{mc_p - m\Delta h\bar{W}}, & A \rightarrow M_d \\ \frac{I^2 R - hS(T-T_\infty)}{mc_p - m\Delta h\bar{H}} & M_d \rightarrow A \end{cases}. \tag{25}$$

It is obvious to see that equations in (25) are already in the form of temperature rate $\dot{T}$ with T as the only variable. However, because $\bar{W}$ and $\bar{H}$ are both nonlinear functions of T, analytical solutions to (25) are not available.

By substituting (25) in (13) and (14), respectively, the strain rates $\dot{\epsilon}$ for cooling and heating processes are formulated as

$$\dot{\epsilon} = \begin{cases} \frac{hS(\Theta + \Omega\bar{W})(T - T_\infty)}{mc_p D - m\Delta h \bar{W} W D}, & A \to M_d \\ \frac{(\Theta + \Omega\bar{H})[hS(T - T_\infty) - I^2 R]}{mc_p D - m\Delta h \bar{H} D} & M_d \to A. \end{cases} \quad (26)$$

2) Heat Transfer Equation for Nonconstant Bias Load SMA Actuator: Similarly, under the condition of nonconstant bias load, the heat transfer equations are formulated as

$A \to M_d$

$$m(c_p + \Delta hWW_T)\dot{T} - m\Delta hWW_\epsilon\dot{\epsilon} = -hS(T - T_\infty) \quad (27)$$

$M_d \to A$

$$m(c_p - \Delta hHa_A)\dot{T} - m\Delta hHH_\epsilon\dot{\epsilon} = I^2 R - hS(T - T_\infty). \quad (28)$$

The heat convection coefficient h depends on the wires' cooling strategies. In this article, we only discuss two types of SMA wire cooling methods: natural convection and forced convection by air flow.

3) Convection Coefficient h: The convection coefficient h for a cylindrical wire in a cross-flow is defined by averaged Nusselt number $\overline{Nu}$, wire diameter d, and air thermal conductivity k_{air} [31]

$$h = \frac{k_{air}\overline{Nu}}{d}. \quad (29)$$

Since k_{air} and d can be easily obtained, finding the averaged Nusselt number $\overline{Nu}$ for both convection methods becomes the major task to determine h. Fortunately, researchers have developed accurate correlation formulas to model $\overline{Nu}$ for various convection conditions.

For natural convection of ahorizontal SMA wire in the air, $\overline{Nu}_N$ can be modeled as [31]

$$\overline{Nu}_N = \left\{ 0.6 + \frac{0.387Ra^{\frac{1}{6}}}{\left[1 + \left(\frac{0.559}{Pr}\right)^{\frac{9}{16}}\right]^{\frac{8}{27}}} \right\}^2. \quad (30)$$

Pr denotes the Prandtl number, which is defined as the ratio of kinematic viscosity ν to the thermal diffusivity α. Ra is the Rayleigh number which is defined as

$$Ra = \frac{g\beta(T - T_\infty)d^3}{\nu\alpha} \quad (31)$$

where g is the gravity acceleration; β denotes the thermal expansion coefficient. The restriction for the valid use of (30) is $Ra \leq 10^{12}$.

For forced convection by moving air, Churchill–Bernstein's model [31] can be employed to calculate $\overline{Nu}_F$ for a horizontal SMA wire in a cross-flow

$$\overline{Nu}_F = 0.3 + \frac{0.62Re^{\frac{1}{2}}Pr^{\frac{1}{3}}}{\left[1 + \left(\frac{0.4}{Pr}\right)^{\frac{2}{3}}\right]^{\frac{1}{4}}} \left[1 + \left(\frac{Re}{282,000}\right)^{\frac{5}{8}}\right]^{\frac{4}{5}}. \quad (32)$$

Re denotes the Reynold number and is formulated as

$$Re = \frac{ud}{\nu} \quad (33)$$

where u represents the air flow speed related to the cylindrical wire. To ensure the modeling accuracy of (32), the production value of RePr has to be no less than 0.2.

C. Numerical Computation of Actuation Frequency

Based on the SMA constitutive model in Section III-A and the SMA heat transfer differential equation in Section III-B, we can derive strain rate $\dot{\epsilon}$ and temperature rate $\dot{T}$ for numerically computing the actuation frequency of SMA actuators. For the case of constant bias load, the rate forms of ϵ and T have been developed in (25) and (26). While for the case of non-constant bias load (i.e. extension spring), $\dot{\epsilon}$ and $\dot{T}$ are derived in (34) and (35) shown at the bottom of this page, by combining (18), (27) and (19), (28). Equations (25), (26) and (34), (35) are two sets of first order nonlinear ODEs that involve a number of parameters. To clarify the proposed method, we illustrate the computation framework in Fig. 2.

The computation framework mainly consists of the following four parts:

1) parameters identification;
2) computation initial conditions;
3) strain-cycling model; and
4) numerical solver.

The parameters used in the strain-cycling model can be categorized as SMA property parameters, actuator design parameters, and control parameters. The SMA property parameters such as zero-stress transformation temperatures (M_f, M_s, A_s, A_f), Young's moduli (D_A, D_M), and specific heat (c_p) are directly determined by the selected materials. Depending on different applications with demanded output forces and stroke distances, parameters of SMA and bias loads can be designed accordingly, such as diameters (d) and lengths (L) of 1-D SMA wires, σ_c for constant bias load, and k, F_i for extension spring bias load. The SMA wire's stress influence coefficients (C_A, C_M) and critical stresses below $(\bar{\sigma}_f, \bar{\sigma}_s)$ are subsequently determined. The actuation control parameters include the input current I for

$$\dot{\epsilon} = \begin{cases} \frac{[-I^2 R + hS(T - T_\infty)](\Theta + \Omega Ha_A)}{m(c_p - \Delta hHa_A)(D + kL/s + \Omega HH_\epsilon) + m\Delta hHH_\epsilon(\Theta + \Omega Ha_A)} & M_d \to A \\ \frac{hS(T - T_\infty)(\Theta - \Omega WW_T)}{m(c_p + \Delta hWW_T)(D + kL/s + \Omega WW_\epsilon) + m\Delta hWW_\epsilon(\Theta - \Omega WW_T)} & A \to M_d \end{cases} \quad (34)$$

$$\dot{T} = \begin{cases} \frac{[I^2 R - hS(T - T_\infty)](D + kL/s + \Omega HH_\epsilon)}{m(c_p - \Delta hHa_A)(D + kL/s + \Omega HH_\epsilon) + m\Delta hHH_\epsilon(\Theta + \Omega Ha_A)} & M_d \to A \\ \frac{-hS(T - T_\infty)(D + kL/s + \Omega WW_\epsilon)}{m(c_p + \Delta hWW_T)(D + kL/s + \Omega WW_\epsilon) + m\Delta hWW_\epsilon(\Theta - \Omega WW_T)} & A \to M_d \end{cases} \quad (35)$$
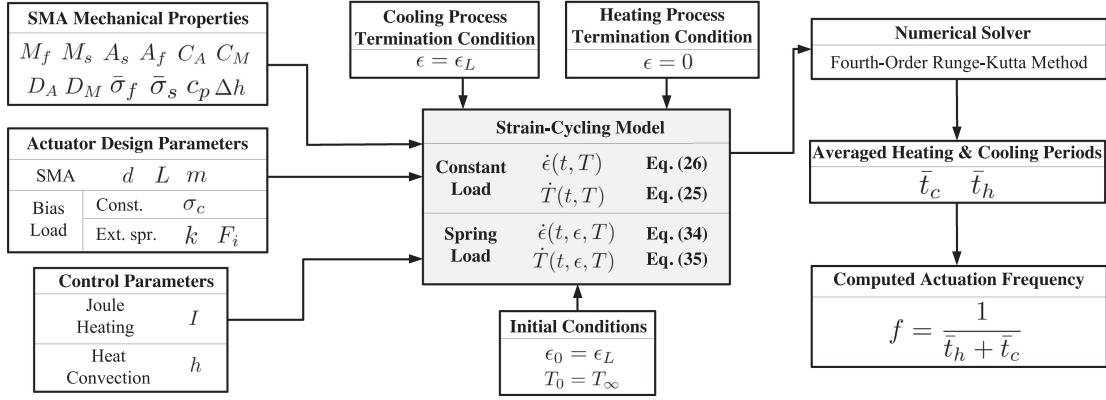
Fig. 2.   1-D SMA actuator strain-cycling frequency computation framework.
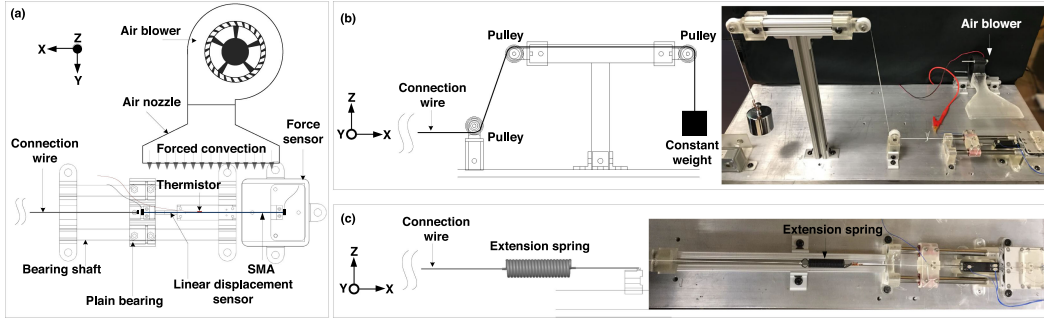

Fig. 3.   Experiment setups for measuring SMA wires' characteristic parameters and evaluating numerically predicted actuation frequency. (a) Conceptual illustration of the experiment system. (b) Experiment setup of constant bias load. (c) Experiment setup of extension spring bias load.

Joule heating and the heat convection coefficient h, which is modeled in Section III-B3.

The strain-cycling models can be treated as initial value problems with the initial conditions $\epsilon_0 = \epsilon_L$ and $T = T_\infty$. For full strain range actuation, $\epsilon = 0$ and $\epsilon = \epsilon_L$ serve as termination conditions for heating process and cooling process, respectively, in each cycle. Considering the nonlinearity of the strain-cycling models, we employ the fourth-order Runge–Kutta method [32] as the numerical solver to approximate the averaged actuation time $\bar{t}_h$ for $M_d \to A$ and $\bar{t}_c$ for $A \to M_d$. Thus, the actuation frequency can be computed as $f = 1/(\bar{t}_h + \bar{t}_c)$.

IV. EXPERIMENTAL VERIFICATION

In this section, experiments are conducted to verify the performance of our proposed numerical model. By changing heat convection methods, Joule heating methods, bias loads, and SMA wire diameters, we investigate how these factors influence the actuation frequency and examine the prediction accuracy.

A. Experiment Platform Setup

Fig. 3 shows the configuration of our experiment platform. A set of HT Flexinol Ni-Ti SMA wires (Dynalloy, Inc.) with different diameters were selected for the experiment. In Fig. 3(a), one SMA terminal was fixed on a force sensor that has a resolution of 0.05N (HEX-58-RB-2000 N, OptoForce, Inc.),

and the other terminal was fixed on a sliding part, which has two linear bearings (FLC06, Pacific Bearing Inc.). The friction between the sliding part and the bearing shafts is below 0.1 N. The linear displacement sensor (LMC13-25, P3 America, Inc.) that features infinite resolution recorded the SMA wire strain during phase transformation. A micromini size thermistor (F μ-3122 Thermistor Assembly, Semitec, Inc.) with 0.28 mm sensor diameter and 0.02 s time constant was employed to measure the SMA wire temperature. The SMA wire was stressed by constant weights [see Fig. 3(c)] and extension springs [see Fig. 3(d)] through a soft and strong nylon wire in connection. The Joule heating of SMA wires was conducted by using a current control system, which consists of a power supply in constant current mode (GW Instek PSW80-27, Good Will Instrument Co., Ltd), a N-Channel MOSFET (RFP30N06LE, Fairchild Semiconductor International, Inc.), and a microcontroller (STM32F4Discovery, STMicroelectronics, Inc.). The thermistor and the linear displacement sensor also provide measurement feedbacks to the microcontroller. Regarding to the forced convection experiments, we adopted an air blower (HT-07530D12, Fugetek Inc.) and designed an air nozzle for generating uniform air flow across the wire. The uniformity of air flow along the SMA wire is measured by using a hot-wire anemometer (STA2, Fieldpiece Instruments, Inc.) and computed as 92.1%. By controlling the input voltages of the air blower, the outlet air flow speed can be adjusted.
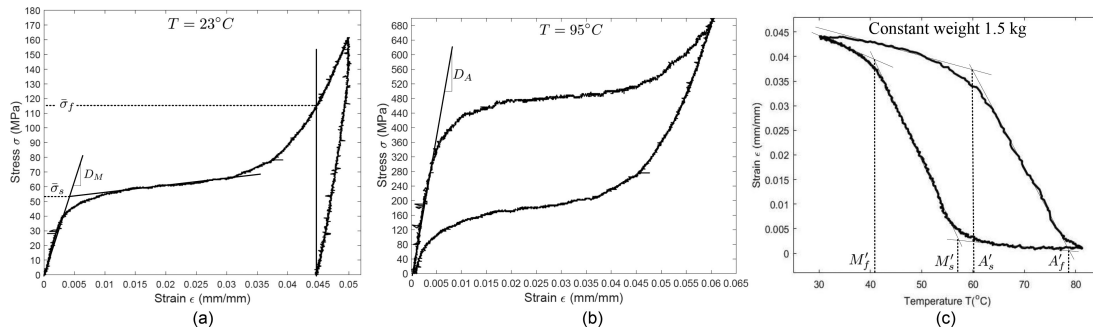
Fig. 4. (a) Isothermal loading and unloading test for the SMA wire with a diameter of 0.375 mm at $T = 23$ °C. (b) Isothermal loading and unloading test for the SMA wire with a diameter of 0.375 mm at $T = 95$ °C. (c) Determination of SMA phase transformation temperatures with 1.5 kg constant weight load.

B. Measurement of SMA Characteristic Parameters

The SMA characteristic parameters such as transformation temperatures (M_f, M_s, A_s, A_f), Young's moduli (D_A, D_M), and critical stresses ($\bar{\sigma}_s, \bar{\sigma}_f$), associate with the SMA material's composition. Once an SMA material is selected, these parameters are relatively consistent from batch to batch. However, these SMA characteristic parameters for our selected material are not provided in the manufacturer's datasheet. Experiments are needed to identify these SMA parameters. Most SMAs have some degree of irreversible behavior, which can be exhausted through actuation cycling. Therefore, all the selected SMA wires in this article were thermomechanically precycled for 100 times under 150 MPa constant stress.

In the following two experiments, an SMA wire with diameter of 0.375 mm and length of 151.3 mm (at the phase of detwinned martensite) was employed.

1) Young's Moduli and Critical Stresses: The Young's moduli D_M and D_A of the SMA wire were measured in isothermal loading and unloading processes that were achieved by replacing the constant weight loads in Fig. 3(b) with a DC motor. The motor was controlled with a rotational speed of 3RPM at 12 V (TS-42GZ495-1622, Tsiny Motor Industrial Co., Ltd). For measuring D_M, the wire was initially kept at the phase of twinned martensite under room temperature 23 °C. By driving the motor clockwise and counterclockwise, the loading and unloading stress-strain curve was recorded in Fig. 4(a). Besides D_M, the critical stresses $\bar{\sigma}_s, \bar{\sigma}_f$ and the maximum recoverable strain ϵ_L were also obtained in Fig. 4(a).

For measuring D_A, the wire was kept at the phase of austenite by controlling the wire temperature at 95 °C, which was achieved by our closed-loop PID temperature control system. Fig. 4(b) shows the stress-strain relationship during the loading-unloading process. The experiments shown in Fig. 4(a) and (b) were carried out multiple times. The measured parameters were averaged as the final results.

2) Zero-Stress Transformation Temperatures: Because the SMA transformation temperatures are stress-dependent, zero-stress values can be acquired by measuring the transformation temperatures at different stress levels. We prepared constant weight loads which are 1.3 kg, 1.5 kg, 1.7 kg, and 1.9 kg to participate in the experiment setup shown in Fig. 3(a) and (b). Four transformation temperatures M_f', M_s', A_s', A_f' under each
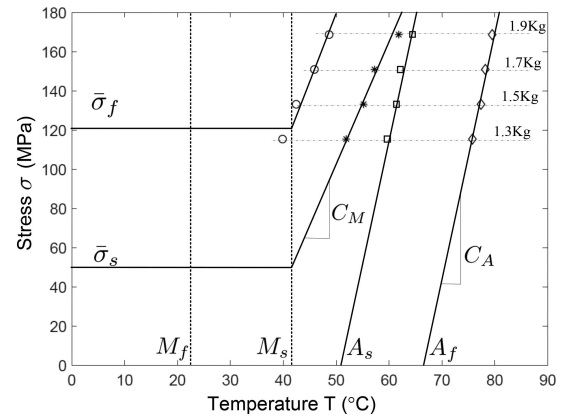

Fig. 5. Determination of zero-stress SMA phase transformation temperatures.

constant weight can be measured. Fig. 4(c) shows an example of using the weight of 1.5 kg. The SMA phase transformation temperatures obtained under different constant weights are plotted in Fig. 5. Zero-stress transformation temperatures M_s, A_s, A_f were extrapolated. M_s was determined by the intersection of $\bar{\sigma}_s$ and the stress-temperature line for M_s according to Brinson's model. The stress influence coefficients C_M and C_A were also obtained in Fig. 5.

The other SMA material related parameters such as latent heat of transformation Δh, thermal coefficient of expansion Θ, and specific heat c_p. can be found in the manufacturer's datasheet [33]. The SMA's characteristic parameters are summarized in Table I.

C. Example Comparison

In this section, we provide a case study for comparing the strain and temperature cycles between our experiment measurements and numerical prediction. We apply a constant stress 124 MPa on an SMA wire with a diameter of 0.375 mm. The input current during the heating process was set at $I = 1.5$ A. The ambient temperature of the SMA wire was 23 °C with natural convection.

Fig. 6(a) shows the strain and temperature cycles obtained from the experiment measurement and numerically computed results for 200 s. The strain cycles start from the phase of

| Property	Value
Martensite finish temperature M_f (°C)	22.1
Martensite start temperature M_s (°C)	41.4
Austenite start temperature A_s (°C)	50.6
Austenite finish temperature A_f (°C)	68.1
Stress influence coefficient C_M (MPa °C^{-1})	6.05
Stress influence coefficient C_A (MPa °C^{-1})	14.25
Young's modulus at 100%austenite D_A (GPa)	71.7
Young's modulus at 100%martensite D_M (GPa)	12.5
Critical stress $\bar{\sigma}_s$ (MPa)	50.6
Critical stress $\bar{\sigma}_f$ (MPa)	120.3
Maximum recoverable strain ϵ_L	0.045
Specific heat c_p (J kg^{-1} °C^{-1})	837.36
Latent heat of transformation Δh (J kg^{-1})	2.42e-4
Thermal expansion coefficient Θ (MPa °C^{-1})	0.5
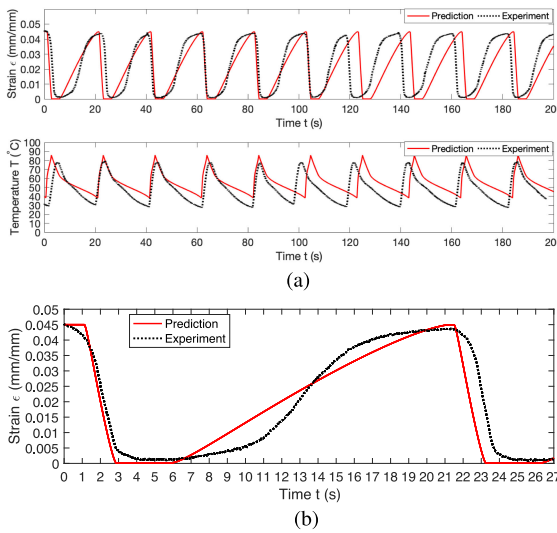
Fig. 6. Comparison of experimental measurements and numerical prediction by using an SMA wire with a diameter of 0.375 mm, 124 MPa constant bias stress, and 1.5 A current for heating process under natural convection. (a) Strain cycles and temperature cycles. (b) Demonstration of one strain cycle.

detwinned martensite with $\epsilon = \epsilon_L$. During the heating process, the strain reduces and ends at $\epsilon = 0$ while the temperature increases. The cooling process starts when $\epsilon = 0$ by cutting off the Joule heating. By natural convection, the SMA wire's temperature reduces and the strain recovers to ϵ_L. We observe that the predicted strain and temperature cycles generally agree with the experimental measurements. The possible reasons of the imperfect match between experimental and prediction data are explained as follows.

In the experiment measurements, the strain and temperature cycles are affected by the reliability of the measurement system and unexpected movements of the actuator's surrounding air especially for natural convection cooling condition. The actuation periods have slight changes from cycle to cycle, as shown in the black dot-lines in Fig. 6(a). For demonstrating the potential error sources, we intentionally includes one cycle in the range of 100–120 s with significantly smaller cycle period compared with the other cycles. This is very likely caused by the occasionally happened misreading of the linear displacement sensor, which

determined to apply current when the phase transformation of $A(\epsilon = 0) \rightarrow M_d(\epsilon = \epsilon_L)$ was unfinished. Therefore, it is necessary to average the measured cycles for comparing with the predicted results.

The temperature-time graph in Fig. 6(a) shows the predicted temperature cycles are higher than the experimental measurements. The possible cause of this difference is the way how the wire temperature was measured, i.e., attaching on the SMA wire side by side. It may not be accurate enough to sense the wire's internal temperature. As the SMA wire diameter gets smaller than the size of the thermistor (0.28 mm in diameter), the error of measured temperature will significantly increase.

Fig. 6(b) shows one cycle comparison of strain-time curves. The red line indicates the predicted strain-time curve starting from the maximum recoverable strain $\epsilon = 0.045$. In the heating process, the predicted strain reaches $\epsilon = 0$ at about 2.8 s. According to the critical stress model in Section III-A2, no phase transformation $A \rightarrow M_d$ happens when $\sigma > \bar{\sigma}_f + C_M(T - M_s)$. As the temperature T reduces during the cooling process, the phase transformation $A \rightarrow M_d$ starts at about 6 s when $\bar{\sigma}_s + C_M(T - M_s) < \sigma < \bar{\sigma}_f + C_M(T - M_s)$. Although the predicted strain-time curve is not perfectly replicating the experiment curve during the cooling process, the proposed model still reveals good capability of predicting strain-cycling time. In the following sections, we further investigate the performance of strain-cycling time prediction by varying design and control parameters.

D. Design of Experiments

The design of our experimental validation involves exploring four design parameters, i.e., SMA wire diameter d, input current density $j = 4I/(\pi d^2)$, bias stress σ, and air flow speed u. Considering two different types of bias stress are modeled in this article, the experiments are categorized into two groups: constant bias loads and extension spring bias loads.

For each design parameter, we have to select a set of testing samples. We employ three SMA wire diameters: 0.2 mm, 0.25 mm, and 0.3 mm. The current densities used in the experiments are 1.2×10^7A m^{-1}, 1.5×10^7A m^{-1}, 1.8×10^7A m^{-1}, 2.0×10^7A m^{-1}. The reason of limiting the maximum current density at 2.0×10^7A m^{-1} is to protect our current control system from being burned by overly large current. The range of bias stress is from 120 to 180 MPa, where 120 MPa is the critical stress $\bar{\sigma}_f$ to guarantee a complete detwinned martensite transformation, as shown in Table I; 180 MPa is determined below the yielding stress of the SMA material to guarantee reliable phase transformation repeatability. For constant load tests, we used four different stresses 120 MPa, 140 MPa, 160 MPa, and 180 MPa. For spring load tests, we paired three different extension springs with the three wire diameters to make sure that the applied bias stresses are in the range of 120–180 MPa: ($d = 0.2$ mm, $k = 0.14$ N·mm^{-1}), ($d = 0.25$ mm, $k = 0.22$ N·mm^{-1}), and ($d = 0.3$ mm, $k = 0.6$ N·mm^{-1}). We set the identical initial stress as 120 MPa for each wire-spring group by applying certain initial extensions on the springs. The air flow speeds used in the experiments were set as 0 m s^{-1}, 0.5 m s^{-1}, 1 m s^{-1}, and 1.5 m s^{-1}.
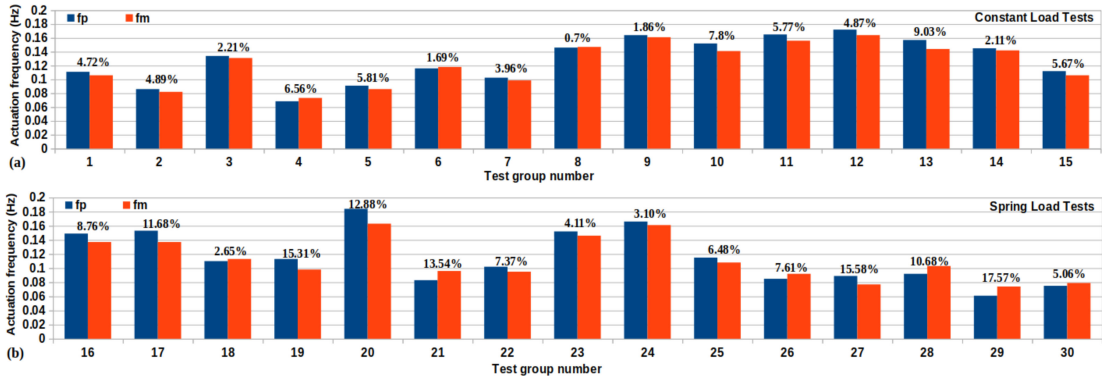
Fig. 7. Strain-cycling frequency comparison between numerical prediction f_p and experimental measurements f_m.

TABLE II
THIRTY TEST GROUPS SAMPLED BY LHS METHOD

ID	d (mm)	σ (MPa)	j (A m^{-2})	u (m s^{-1})
1	0.3	180	1.5e7	0.5
2	0.3	160	1.2e7	1.5
3	0.3	160	1.8e7	0.5
4	0.3	140	2.0e7	0
5	0.3	140	1.5e7	0.5
6	0.25	180	2.0e7	0
7	0.25	120	1.5e7	0.5
8	0.25	120	1.8e7	1
9	0.25	180	1.8e7	1.5
10	0.25	120	1.8e7	1.5
11	0.2	160	2.0e7	1
12	0.2	180	2.0e7	1
13	0.2	120	2.0e7	0.5
14	0.2	180	2.0e7	0
15	0.2	140	1.8e7	0

ID	d (mm), k (N mm^{-1})	j (A m^{-2})	u (m s^{-1})
16	0.20, 0.14	1.8e7	1
17	0.20, 0.14	2.0e7	0.5
18	0.20, 0.14	1.8e7	0
19	0.20, 0.14	2.0e7	0
20	0.20, 0.14	2.0e7	1
21	0.25, 0.22	2.0e7	0
22	0.25, 0.22	1.5e7	0.5
23	0.25, 0.22	1.8e7	1
24	0.25, 0.22	1.8e7	1.5
25	0.25, 0.22	1.5e7	1.5
26	0.30, 0.60	1.5e7	0.5
27	0.30, 0.60	1.2e7	1
28	0.30, 0.60	1.8e7	0.5
29	0.30, 0.60	2.0e7	0
30	0.30, 0.60	1.2e7	0.5

The total combination number of the constant load tests is $3(d) \times 4(\sigma) \times 4(j) \times 4(u) = 192$ while the total combination number of the spring load tests is $3(d, \sigma) \times 4(j) \times 4(u) = 48$. To efficiently run the experiments over the 240 combinations, we adopt latin hypercube sampling (LHS) method [34] to sample 30 combinations (15 samples for constant loads, 15 samples for spring loads) to represent the design space, as shown in Table II.

E. Strain-Cycling Frequency Analysis

Fig. 7 shows the comparison results between the numerically predicted actuation frequency f_p (blue bars) and experimentally measured frequency f_m (red bars) according to Table II. The groups 1 to 15 are constant load tests while the groups 16 to 30 are spring load tests. f_m is the averaged frequency of actuation for in each test. The percentage differences between f_p and f_m

are shown in the bar plots for each group. The results in Fig. 7(a) show a minimum percentage difference of 0.7% and a maximum percentage difference of 9.03% for constant load tests. While for spring load tests in Fig. 7(b), a minimum percentage difference of 2.65% and a maximum percentage difference of 17.57% are indicated.

In order to investigate if the performance of actuation frequency prediction in Fig. 7(a) and (b) is significantly different, a two sample t-test was conducted by reasonably assuming 1) the tests in Fig. 7(a) and (b) are independent; and 2) the percentage differences in Fig. 7(a) and (b) follow a normal distribution without knowing the variance. The null hypothesis is defined as $H_0 : \mu_c = \mu_s$, which represents the mean values of percentage difference for constant and spring load tests. The level of marginal significance p can thus be computed as $p = 9.7e{-4}$ that rejects the null hypothesis at the significant level of $\alpha = 0.01$. The result indicates that the numerical model provides more accurate actuation frequency prediction for constant load SMA actuators than that for spring load SMA actuators. This is very likely caused by introducing (12) in the spring load model, which increases numerical errors.

F. Sensitivity Analysis of Numerical Model

The proposed numerical model involves using predetermined parameters of SMA mechanical properties, i.e., $M_f, M_s, A_s, A_f, C_A, C_M, D_A, D_M, \bar{\sigma}_f, \bar{\sigma}_s, c_p$, and Δh. To gain more insights of the proposed model, we investigate how the uncertainties of these parameters affect the predicted actuation frequency of a 1-D SMA actuator.

In order to conduct this task, the variation range of each parameter is $\pm 10\%$ of its measured value in Table I. For each parameter, we evenly collect 21 samples within its range, and numerically compute the predicted actuation frequency f_p of one parameter by setting the other parameters as the measured values. The actuator design parameters (d, L, m) and control parameters (I, h) are set identical to the values used in Section IV-C.

Fig. 8 shows the sensitivity analysis results. The slopes of the linear fitting lines in Fig. 8 indicate the correlations between the parameters and the predicted actuation frequency f_p. Among the zero-stress phase transformation temperatures, the magnitudes of $\partial f_p / \partial M_s$ and $\partial f_p / \partial A_f$ in Fig. 8(b) and (d) are at 10^{-3} and
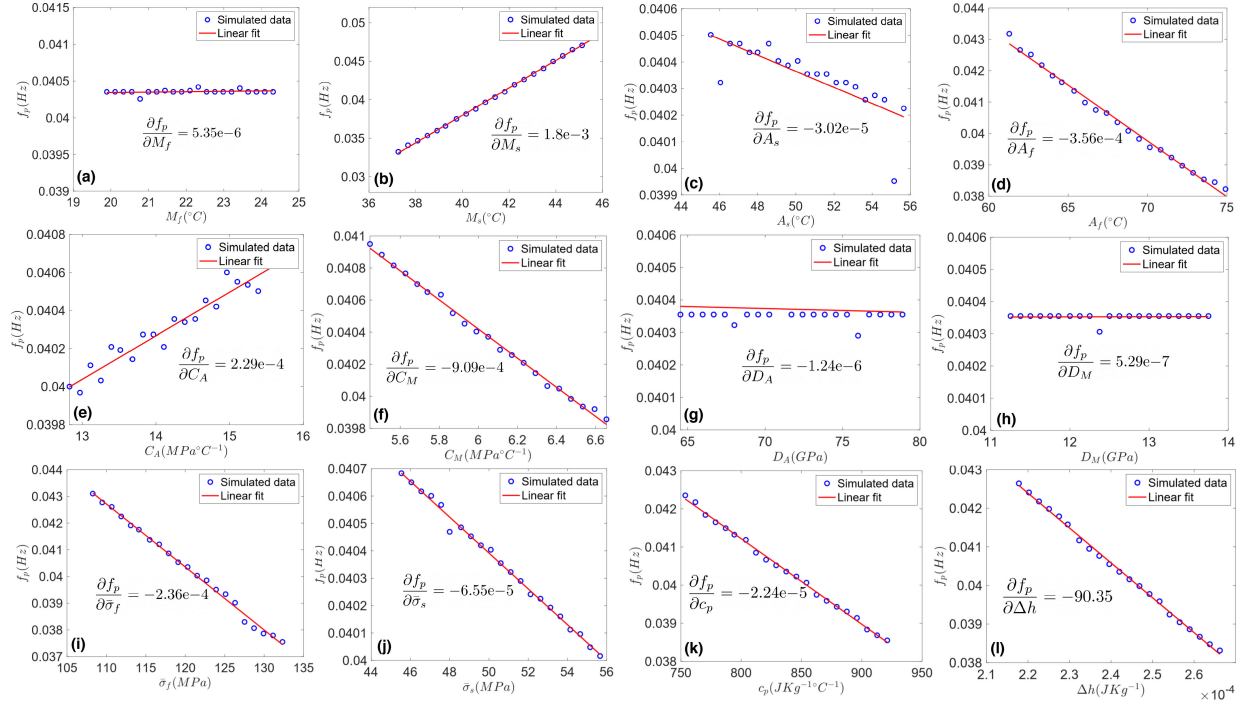
Fig. 8. Design parameters sensitivity analysis of the actuation frequency prediction model. (a) $f_p - M_f$ plot. (b) $f_p - M_s$ plot. (c) $f_p - A_s$ plot. (d) $f_p - A_f$ plot. (e) $f_p - C_A$ plot. (f) $f_p - C_M$ plot. (g) $f_p - D_A$ plot. (h) $f_p - D_M$ plot. (i) $f_p - \bar{\sigma}_f$ plot. (j) $f_p - \bar{\sigma}_s$ plot. (k) $f_p - c_p$ plot. (l) $f_p - \Delta h$ plot.

10^{-4}, respectively, which are higher than those of $\partial f_p / \partial M_f$ and $\partial f_p / \partial A_s$, as shown in Fig. 8(a) and (c). The results indicate that M_s and A_f have stronger correlations with f_p than M_f and A_s. This can be reflected in (5) and (7) where M_s and A_s are directly used for modeling the martensite fraction during cooling and heating processes. By using similar interpretation, C_A, C_M, and $\bar{\sigma}_f$ [in Fig. 8(e), (f), and (i)] show the same correlation level with f_p as A_f, while $D_A, D_M, \bar{\sigma}_s, c_p$ [in Fig. 8(g), (h), (j), (k)] demonstrate weaker correlations with f_p as M_f, A_s. $\partial f_p / \partial \Delta h$ demonstrates the highest magnitude in Fig. 8. The latent heat of transformation Δh for an SMA wire is usually provided by its manufacturer [33]. So we can reasonably assume this value is accurately measured.

G. Limitation and Discussion

Due to the limitation of the maximum current capacity of our experiment system, which restricts the selection of SMA wire diameters as well, this article only covers the verification of the numerical model for predicting the actuation frequencies within the range of 0.06–0.2 Hz. For applications that require frequencies of SMA actuators outside this range, further verification of the numerical model is needed.

The modeling of SMA actuators with magnetic bias stress [see Fig. 1(d)] is not provided in this article considering that the modeling method is similar to the SMA actuators with spring bias stress. In the experimental evaluation, we found the numerical model of spring loads yielded higher numerical errors than that of constant loads. The strain-stress relation of SMA actuators with magnetic bias stress can be modeled by polynomial curves, which result in higher nonlinearity than that

of SMA actuators with spring loads. The numerical predication accuracy in this case could be further degraded. In addition, in this article, we reply on the Brinson's model to describe the stress-temperature relation of 1-D SMA wires, which involves of premeasuring ten parameters as presented in Section IV-B. According to the sensitivity analysis in Section IV-F, the measurement accuracy of these parameters affects prediction performance. One alternative way to bypass the proposed model based method is to use machine learning (ML) based methods. However, the downside of using ML based methods is that the requirement of sufficient training data demands tremendous effort on conducting experiments.

V. CONCLUSION

To develop 1-D SMA actuators with desired strain-cycling frequencies, we develop a versatile numerical model, which takes various heating convection methods, bias loads, and Joule heating methods as the model inputs, to predict actuation frequencies according to different design configurations. The proposed numerical model effectively integrates the SMA constitutive model, an SMA phase transformation kinetic model, stress-strain models, and the SMA wire heat transfer model. A total of 30 experimental tests generated by the LHS method were conducted to evaluate accuracy of the predicted strain-cycling frequencies. The design parameters in the tests include constant bias load, SMA wire diameter, input current density, nonconstant bias load, convection air speed. The experiment results demonstrate that within the actuation frequency range of 0.06–0.2 Hz, the numerically predicted frequencies show percentage

differences of 0.7%–9.03% (constant loads) and 2.65%–17.57% (spring loads) with respect to the measured values.

References

[1] J. M. Jani, M. Leary, A. Subic, and M. A. Gibson, "A review of shape memory alloy research, applications and opportunities," *Mater. Des.*, vol. 56, pp. 1078–1113, 2014.

[2] K. Melton, "Ni-ti based shape memory alloys," in *Engineering Aspects of Shape Memory Alloys*. Oxford, U.K.: Butterworth-Heinemann, 1990, pp. 21–35.

[3] S. Kim, E. Hawkes, K. Choy, M. Joldaz, J. Foleyz, and R. Wood, "Micro artificial muscle fiber using NiTi spring for soft robotics," in *Proc. IEEE/RSJ Int. Conf. Intell. Robots Syst.*, Oct. 2009, pp. 2228–2234.

[4] B. Konh, S. Karimi, and S. Miller, "Feasibility study of an active soft catheter actuated by SMA wires," *Proc. SPIE*, vol. 10602, 2018, Art. no. 106020C.

[5] G. Mani, M. D. Feldman, D. Patel, and C. M. Agrawal, "Coronary stents: A materials perspective," *Biomaterials*, vol. 28, no. 9, pp. 1689–1710, 2007.

[6] L. Blanc, A. Delchambre, and P. Lambert, "Flexible medical devices: Review of controllable stiffness solutions," *Actuators*, vol. 6, no. 3, pp. 23–54, 2017.

[7] H. Rodrigue, W. Wang, M.-W. Han, T. J. Kim, and S.-H. Ahn, "An overview of shape memory alloy-coupled actuators and robots," *Soft Robot.*, vol. 4, no. 1, pp. 3–15, 2017.

[8] M. Leary, S. Huang, T. Ataalla, A. Baxter, and A. Subic, "Design of shape memory alloy actuators for direct power by an automotive battery," *Mater. Des.*, vol. 43, pp. 460–466, 2013.

[9] D. J. Hartl and D. C. Lagoudas, "Aerospace applications of shape memory alloys," *Proc. Inst. Mech. Engineers, Part G: J. Aerosp. Eng.*, vol. 221, no. 4, pp. 535–552, 2007.

[10] C. Liang and C. Rogers, "One-dimensional thermomechanical constitutive relations for shape memory materials," *J. Intell. Mater. Syst. Struct.*, vol. 1, no. 2, pp. 207–234, 1990.

[11] F. Taylor and C. Au, "Forced air cooling of shape-memory alloy actuators for a prosthetic hand," *J. Comput. Inf. Sci. Eng.*, vol. 16, no. 4, 2016, Art. no. 041004.

[12] S. S. Cheng, Y. Kim, and J. P. Desai, "Modeling and characterization of shape memory alloy springs with water cooling strategy in a neurosurgical robot," *J. Intell. Mater. Syst. Struct.*, vol. 28, no. 16, pp. 2167–2183, 2017.

[13] R. A. Russell and R. B. Gorbet, "Improving the response of SMA actuators," in *Proc. IEEE Int. Conf. Robot. Autom.*, vol. 3, pp. 2299–2304, 1995.

[14] A. R. Shahin, P. H. Meckl, J. D. Jones, and M. A. Thrasher, "Enhanced cooling of shape memory alloy wires using semiconductor "heat pump" modules," *J. Intell. Mater. Syst. Struct.*, vol. 5, no. 1, pp. 95–104, 1994.

[15] P. Motzki, T. Gorges, M. Kappel, M. Schmidt, G. Rizzello, and S. Seelecke, "High-speed and high-efficiency shape memory alloy actuation," *Smart Mater. Struct.*, vol. 27, no. 7, 2018, Art. no. 075047.

[16] A. Lara-Quintanilla and H. E. N. Bersee, "Active cooling and strain-ratios to increase the actuation frequency of SMA wires," *Shape Memory Superelasticity*, vol. 1, pp. 460–467, Dec. 2015.

[17] W. Huang, *Shape Memory Alloys and Their Application to Actuators for Deployable Structures*. Ph.D. dissertation, Engineering Department, Cambridge University, Cambridge, U.K., 1998.

[18] Z. Guo, Y. Pan, L. B. Wee, and H. Yu, "Design and control of a novel compliant differential shape memory alloy actuator," *Sensors Actuators A: Phys.*, vol. 225, pp. 71–80, 2015.

[19] Y. Tadesse, N. Thayer, and S. Priya, "Tailoring the response time of shape memory alloy wires through active cooling and pre-stress," *J. Intell. Mater. Syst. Struct.*, vol. 21, no. 1, pp. 19–40, 2010.

[20] X. Liu, H. Liu, and J. Tan, "Mesoscale shape memory alloy actuator for visual clarity of surgical cameras in minimally invasive robotic surgery," *IEEE Trans. Med. Robot. Bionics*, vol. 1, no. 3, pp. 135–144, Aug. 2019.

[21] A. Bhattacharyya, L. Sweeney, and M. G. Faulkner, "Experimental characterization of free convection during thermal phase transformations in shape memory alloy wires," *Smart Mater. Struct.*, vol. 11, no. 3, pp. 411–422, 2002.

[22] S. Huang, M. Leary, T. Ataalla, K. Probst, and A. Subic, "Optimisation of Ni'Ti shape memory alloy response time by transient heat transfer analysis," *Mater. Des.*, vol. 35, pp. 655–663, 2012.

[23] L. Brinson, "One-dimensional constitutive behavior of shape memory alloys: Thermomechanical derivation with non-constant material functions and redefined martensite internal variable," *J. Intell. Mater. Syst. Struct.*, vol. 4, no. 2, pp. 229–242, 1993.

[24] Y. Lu, R. Zhang, Z. Xie, H. Yue, and L. Wang, "A new variable speed phase transformation constitutive model of shape memory alloys," *Mater. Res. Exp.*, vol. 6, Aug. 2019, Art. no. 105705.

[25] A. Pathak, D. Brei, and J. Luntz, "Transformation strain based method for characterization of convective heat transfer from shape memory alloy wires," *Smart Mater. Struct.*, vol. 19, no. 3, 2010, Art. no 035005.

[26] S. Vollach, D. Shilo, and H. Shlagman, "Mechanical response of shape memory alloys under a rapid heating pulse-Part II," *Exp. Mech.*, vol. 56, pp. 1465–1475, 2016.

[27] S. S. Nakshatharan, K. Dhanalakshmi, and D. J. S. Ruth, "Effect of stress on bandwidth of antagonistic shape memory alloy actuators," *J. Intell. Mater. Syst. Struct.*, vol. 27, no. 2, pp. 153–165, 2016.

[28] K. Tanaka, "A thermomechanical sketch of shape memory effect: One-dimensional tensile behavior," *Res. Mechanica*, vol. 18, pp. 251–263, 1986.

[29] L. C. Brinson and M. S. Huang, "Simplifications and comparisons of shape memory alloy constitutive models," *J. Intell. Mater. Syst. Struct.*, vol. 7, no. 1, pp. 108–114, 1996.

[30] D. Cui, G. Song, and H. Li, "Modeling of the electrical resistance of shape memory alloy wires," *Smart Mater. Struct.*, vol. 19, no. 5, 2010, Art. no. 055019.

[31] F. P. Incropera, *Fundamentals Heat and Mass Transfer*. Hoboken, NJ, USA: Wiley, 2006.

[32] J. Butcher, *Numerical Methods for Ordinary Differential Equations*. Hoboken, NJ, USA: Wiley, 2003.

[33] "Technical Characteristics of FLEXINOL Actuator Wires," Accessed: Jan. 20, 2019. [Online]. Available: http://www.dynalloy.com/pdfs/TCF1140.pdf.

[34] B. Tang, "Orthogonal array-based latin hypercubes," *J. Amer. Statist. Assoc.*, vol. 88, no. 424, pp. 1392–1397, 1993.

Xiaolong Liu received the Ph.D. degree in biomedical engineering from the University of Tennessee, Knoxville, TN, USA, in 2015.

He is currently an Assistant Research Scientist with the Department of Mechanical Engineering, Johns Hopkins University, Baltimore, MD, USA. Before joining the University of Maryland, he was a Research Engineer with the AUBO Robotics, Inc., Knoxville, TN, USA, and an Adjunct Faculty with the University of Tennessee. His current research interests include surgical robotics, medical devices, magnetic manipulation, and design optimization.

Hui Liu received the M.S. degree in mechanical engineering from Beihang University, China, in 2018. He is currently working toward the Ph.D. degree in mechanical engineering with the University of Tennessee, Knoxville, TN, USA.

His research interests include medical devices, shape memory actuators and computer vision.
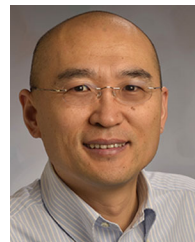
Jindong Tan (Member, IEEE) received the Ph.D. degree in electrical and computer engineering from Michigan State University, East Lansing, MI, USA, in 2002.

He is currently a Professor with the Department of Mechanical, Aerospace and Biomedical Engineering, University of Tennessee, Knoxville, TN, USA. He is also the President and CEO of AUBO Robotics, Inc. He has been an Assistant/Associate Professor with the Department of Electrical and Computer Engineering, Michigan Technological University, Houghton, MI, USA. His current research interests include mobile sensor networks, augmented reality and biomedical imaging, dietary assessment, and mobile manipulation.